

The iridium double perovskite Sr_2YIrO_6 revisited: A combined structural and specific heat study

L.T. Corredor^{1,*}, G. Aslan-Cansever^{1*}, M. Sturza^{1*}, Kaustuv Manna¹,
A. Maljuk¹, S. Gass¹, A. Zimmermann¹, T. Dey¹, C. G. F. Blum¹,
M. Geyer¹, A. U. B. Wolter¹, S. Wurmehl^{1,2}, and B. Büchner^{1,2}

¹*Leibniz Institute for Solid State and Materials Research IFW,
Institute for Solid State Research, 01069 Dresden, Germany and*

²*Institute for solid state physics, Technische
Universität Dresden, D-01062 Dresden, Germany*

(Dated:)

Abstract

Recently, the iridate double perovskite Sr_2YIrO_6 has attracted considerable attention due to the report of unexpected magnetism in this Ir^{5+} ($5d^4$) material, in which according to the J_{eff} model, a non-magnetic ground state is expected. However, in recent works on polycrystalline samples of the series $\text{Ba}_{2-x}\text{Sr}_x\text{YIrO}_6$ no indication of magnetic transitions have been found. We present a structural, magnetic and thermodynamic characterization of Sr_2YIrO_6 single crystals, with emphasis on the temperature and magnetic field dependence of the specific heat. Here, we demonstrate the clue role of single crystal X-ray diffraction on the structural characterization of the Sr_2YIrO_6 double perovskite crystals by reporting the detection of a $\sqrt{2}a \times \sqrt{2}a \times 1c$ supercell, where a , b and c are the unit cell dimensions of the reported monoclinic subcell. In agreement with the expected non-magnetic ground state of Ir^{5+} ($5d^4$) in Sr_2YIrO_6 , no magnetic transition is observed down to 430 mK. Moreover, our results suggest that the low temperature anomaly observed in the specific heat is not related to the onset of long-range magnetic order. Instead, it is identified as a Schottky anomaly caused by paramagnetic impurities present in the sample, of the order of $n \sim 0.5(2)$ %. These impurities lead to non-negligible spin correlations, which nonetheless, are not associated with long-range magnetic ordering.

* these authors contributed equally to this work.

I. INTRODUCTION

The effect of spin-orbit coupling (SOC) on strongly correlated electron systems has demonstrated to be the origin of novel phases [1, 2], like spin liquids [3], unconventional magnetism [4, 5], and topological phases [6], among others. Also, it has been demonstrated that for an intermediate strength regime, SOC can work together with Coulomb interactions to enhance the electron correlations, leading to spin-orbit driven Mott insulators [7, 8]. The key point is that small changes in these interactions can lead to an enormous variety in the electronic and magnetic behaviors. Specifically in $5d$ transition metals like Ir the SOC is significant, and comparable to the atomic interactions like crystal electric field Δ and the on-site Coulomb interaction U . Examples for this scenario are the pyrochlore iridates, which show novel phases like Weyl semimetals [9–11], topological Mott insulators [12, 13], and axion insulators with unusual electromagnetic responses [14, 15].

The most common oxidation states of iridium are 3+ and 4+. On the other hand oxidation states of 5+ and 6+ are rare and sometimes poorly characterized [16]. The double perovskite structure $R_2MM'O_6$ may host iridium on the M and/or M' position; Ir will be in octahedral coordination in this structure type. Hence, the octahedral crystal electric field splits the $5d$ levels in a t_{2g} triplet and a e_g doublet. Then, for Ir^{4+} ($5d^5$ electronic configuration) the large SOC acts on the t_{2g} levels, splitting them into an effective $j = 1/2$ doublet and an effective $j = 3/2$ quartet [17, 18].

According to the strong spin-orbit coupling J_{eff} model, a non-magnetic $j = 0$ ground state is expected for double perovskites with Ir^{5+} ($5d^4$) as the formal oxidation state. That is the case for the monoclinic Sr_2YIrO_6 , synthesized for the first time by Wakeshima et al. [19] in 1999 with the aim of studying the magnetic properties of $5d$ transition metal oxides in which the metal ions are in an unusual oxidation state. As expected, no transition into a long-range ordered state was observed. However, recently a report by Cao et al. on this system [20] reports that a strong non-cubic crystal field (due to the flattening of the IrO_6 octahedra) together with an “intermediate-strength” spin-orbit coupling, leads to a different ground-state configuration, i.e. an antiferromagnetic ground state with $T_N = 1.3$ K. The emergence of magnetic ordering was evidenced in magnetization studies at 7 T as well as in specific heat measurements in different applied magnetic fields. For the latter characterization, a small anomaly in the low temperature region was interpreted as a

signature of long-range magnetic ordering.

Recent first-principles calculations [21] on both Sr_2YIrO_6 and Ba_2YIrO_6 compounds gave another explanation for this behavior. In Ref [21] the authors argue that the breakdown of the $J = 0$ state in Sr_2YIrO_6 would be due to a band structure effect rather than the non-cubic crystal field effect. However, a posterior report by Pajskr et al. [22] combining several numerical and semianalytical methods to study the band structure of both compounds contradicts the conclusions of Refs. [20] and [21]. They found that monoclinic Sr_2YIrO_6 and cubic Ba_2YIrO_6 are quite similar, and that both exhibit no tendency towards a magnetic phase transition at low temperatures.

More recent works on polycrystalline samples of the series $\text{Ba}_{2-x}\text{Sr}_x\text{YIrO}_6$ [23, 24] did not observe any signature for long-range magnetic order in this material in their magnetic susceptibility characterization, in strong contrast with Cao et al [20]. On the contrary, these reports reinforce the notion of a non-magnetic ground state dominated by strong SOC. In both reports [23, 24] the magnetic characteristics of the system do not change significantly across the series, and the effective magnetic moment per Ir is much less than the value expected for a $S = 1$ system as reported by Cao et al. [20], demonstrating a strongly SOC dominated ground state.

In this work, in order to settle the dispute described above, we present a combined structural, magnetic and thermodynamic characterization of Sr_2YIrO_6 single crystals. Structure and composition of the crystals were thoroughly characterized by single crystal X-ray diffraction (XRD), synchrotron powder XRD, energy dispersive X-ray spectroscopy (EDX) and scanning electron microscopy (SEM). The single crystal XRD data show evidence of a cubic supercell. We particularly analyze the specific heat of this material, in order to study the anomaly reported in [20]. In our studies no long-range magnetic order was found even in fields up to 9 T. The magnetic contribution to the specific heat was extracted, finding a Schottky anomaly due to a small amount of magnetic impurities. Further analysis suggests non-negligible spin correlations, which nonetheless, are not associated with long-range magnetic ordering.

II. EXPERIMENTAL DETAILS

A. Crystal growth

Single crystals of Sr_2YIrO_6 were flux-grown using SrCO_3 (Alfa Aesar, 99.994%), Y_2O_3 (Alfa Aesar, 99.99%) and IrO_2 (Alpha Aesar, 99.99%) as the precursor materials. Anhydrous SrCl_2 (Alpha Aesar, 99.5%) was used as the flux. The stoichiometric amount of starting materials and the flux were mixed using a nutrient to solvent weight ratio 1:13. All constituents were put in a platinum crucible (50 cubic ml) with a platinum lid. The crucible edge and lid were squeezed to semi-seal the crucible assembly. The set-up was heated to different high temperatures (1200°C, 1250°C and 1300°C), held for 24 h and then cooled to 900°C with different cooling rates (0.5°C/h, 1°C/h and 2°C/h). The furnace was switched off afterwards and cooled to room temperature.

The crystals were found at the bottom of the crucible and were separated by dissolving the flux in water. After that, in order to gain a better understanding of the growth, the Sr_2YIrO_6 crystals were examined by optical microscopy. As depicted in Figure S1 [25], crystals have different morphologies: cubic-like or irregular polyhedral. The cubic ones correspond to the pure Sr_2YIrO_6 phase and the irregular ones seem to be cubic crystals inter-grown with each other due to additional nucleation sites. All our attempts to avoid the co-crystallization of irregular shaped crystals by varying the hold temperatures, cooling rates and material to flux ratio have been failed. For the following studies, we used the samples grown by cooling down from 1200°C to 900°C with a rate of 2°C/h and material to flux ratio of 1:13.

B. Characterization

A bunch of single crystals of Sr_2YIrO_6 with different morphologies were selected and mounted on the tip of a glass fiber for X-ray Diffraction (XRD). Intensity data were collected at room temperature using ω scans on a STOE imaging plate diffraction system (IPDS-II) with graphite-monochromatized Mo $K\alpha$ radiation ($\lambda = 0.71069 \text{ \AA}$) operating at 50 kV and 40 mA using a 34 cm diameter imaging plate. Individual frames were collected with a 4 min exposure time and a $0.8^\circ\omega$ rotation. X-Area, X-RED, and X-SHAPE software packages [26] were used for data collection, integration, and analytical absorption corrections, respectively. SHELXL [27] and JANA2006 [28] software packages were used to solve and

refine the structure.

High-resolution synchrotron powder diffraction data were collected at the beamline P02.1 at the storage ring PETRA III (DESY, Hamburg, Germany) using an average wavelength of 0.2067 Å (~ 60 keV), with a relative energy bandwidths $\Delta E/E$ of the order of 10^{-4} . The repeatability of the detector translations along the beam was tested in a series of exposures of a LaB₆ standard (NIST 660a) filled into a 0.8 mm-diameter capillary. During this measurement, the detector was moved forward and backward (with and without backlash) over the entire travel range in steps of 125 μ m [29]. The synchrotron powder XRD pattern was collected on crushed single crystals of Sr₂YIrO₆ sealed in a 0.8 mm-diameter capillary. Data were fitted by the Rietveld method [30] using Fullprof in the WinPlotR program package [31].

The microstructural and compositional analysis was performed using scanning electron microscopy (SEM, Zeiss EVOMA15) along with an electron microprobe analyzer for semi-quantitative elemental analysis in the energy dispersive x-ray (EDX) mode (X-MaxN20 detector from Oxford Instruments with a AZtecEnergy Advanced acquisition and EDX analysis software).

The magnetization as a function of temperature (in the range 0.43 - 300 K) and magnetic field was obtained for randomly oriented single crystals of Sr₂YIrO₆ (~ 92.5 mg) using a Superconducting Quantum Interference Device (SQUID) magnetometer from Quantum Design, equipped with an *iHelium3* option. A thorough background subtraction was performed for all the curves. Specific heat measurements were performed on 29 single crystals (~ 5.6 mg) between 0.4 K and 10 K using a heat-pulse relaxation method in a Physical Properties Measurement System (PPMS) from Quantum Design. The heat capacity of the sample holder (addenda) was determined prior to the measurements for the purpose of separating the heat capacity contribution of the sample from the total heat capacity.

III. RESULTS AND DISCUSSION

Sr₂YIrO₆ orders in the double perovskite type structure with the general formula R₂MM'O₆, wherein R denotes an alkaline-earth (or rare-earth) metal and M and M' are d-block elements (or other metals). Double perovskites crystallize in a cubic, tetragonal, or monoclinic symmetry with interpenetrating M and M' face-centered cubic (FCC) sub-

lattices. We started the analysis of Sr_2YIrO_6 single crystal XRD data using the reported monoclinic structural model [20], with the space group $P2_1/n$ and lattice parameters: $a = 5.7826(5) \text{ \AA}$, $b = 5.7830(5) \text{ \AA}$, $c = 8.1746(7) \text{ \AA}$, $\beta = 90.036(7)^\circ$. The single crystal XRD refinement leads to the agreement factors of $R_{obs} = 4.17 \%$ (for $I > 2\sigma(I)$) and $R_{all} = 9.19 \%$.

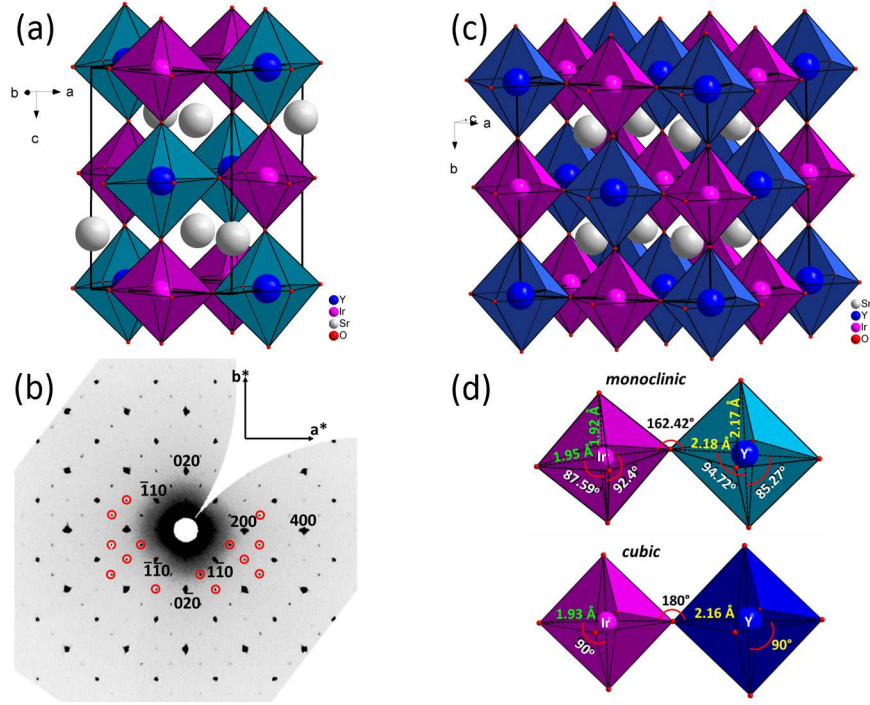


FIG. 1. (Color online) Structural details for Sr_2YIrO_6 crystals: (a) Perspective view of the double perovskite structure of the monoclinic subcell along the crystallographic b axis. (b) Reconstructed precession photographs for Sr_2YIrO_6 crystal in the $hk0$ layers show extra reflections, marked with red circles, required to describe a $\sqrt{2} \times \sqrt{2} \times 1$ supercell. (c) Perspective view of the double perovskite structure of the $\sqrt{2} \times \sqrt{2} \times 1$ cubic supercell along the crystallographic c axis. (d) Comparison between bond lengths and bond angles of the IrO_6 and YO_6 octahedra, monoclinic vs cubic.

After an anisotropic refinement of all atoms, a difference electron density Fourier map calculated with phases based on the final parameters shows maximum and minimum residual peaks of $+2.03$ and -2.58 e\AA^{-3} , respectively. A detailed examination of reconstructed precession images of the $hk0$ layer (Figure 1(b)) shows strong diffraction maxima due to the small subcell and additional weak peaks forming distinctive groups of four reflections around

the allowed peaks. All those extra peaks can be indexed with the $\sqrt{2}a \times \sqrt{2}b \times 1c$ supercell, where a , b and c are the unit cell dimensions of the monoclinic subcell. The integrated data with the $\sqrt{2}a \times \sqrt{2}b \times 1c$ supercell suggests that Sr_2YIrO_6 crystallizes in the cubic space group $Fm\bar{3}m$ with lattice parameter, $a = 8.1773(7)$ Å.

The crystal structure of the supercell based on our refinement, shown in Figure 1(c), is built up of corner-sharing IrO_6 and YO_6 octahedra units, which feature an ordered rock-salt like arrangement, and the Sr placed in between. Please note that the Ir^{5+} ions in this structure build up a FCC network, a general feature of the double perovskite type structure. The single crystal XRD refinement by taking into account the supercell shows excellent agreement factors of $R_{obs} = 1.65$ % (for $I > 2\sigma(I)$) and $R_{all} = 3.79$ % and less electron density difference after an anisotropic refinement of all atoms, i.e. maximum and minimum residual peaks $+1.06$ and -0.98 eÅ⁻³, respectively. The parameters for data collection and the details of the structure refinement are given in Table I. Atomic coordinates, thermal displacement parameters (U_{eq}) and occupancies of all atoms are given in Table II. Anisotropic displacement parameters (ADPs) and selected bond lengths and angles are given in the supplemental material, Tables S1 and S2 [25].

In the Sr_2YIrO_6 subcell, the monoclinic distortion is very small, as presented in Figure 1(d), with β angles very close to 90° ($\beta = 90.036(7)^\circ$) and unequal Ir-O bond lengths with a small difference of 0.03 Å, while $\angle\text{O-Ir-O}$ deviates from 90° by 2.4° , and the IrO_6 octahedra are rotated/tilted with $\angle\text{Ir-O-Y}$ of 162.42° . For our Sr_2YIrO_6 supercell, the IrO_6 octahedra are completely regular with equal Ir-O bond lengths, $\angle\text{O-Ir-O} = 90^\circ$ and $\angle\text{Ir-O-Y} = 180^\circ$. Our experimental results on single crystal XRD are in good agreement with the theoretical paper reported by Pajskr et al. [22], which claims that the non-cubic crystal field of Sr_2YIrO_6 is found to be rather weak and that Sr_2YIrO_6 is quite similar in terms of structure and low-energy properties to the cubic Ba_2YIrO_6 analog [32].

The results of our Rietveld refinement, agreement factors, and refined lattice constants of synchrotron powder XRD ($\lambda = 0.2067$ Å) patterns of the Sr_2YIrO_6 sample studied in this work are shown in the supplemental material [25]. Figure S2 shows the experimental synchrotron XRD data, the simulated and residual intensities as well as the corresponding Bragg positions using the monoclinic structure model. A tiny trace of unreacted Y_2O_3 (~ 1.06 %) is observed. The analysis of the structural data reveals that Sr_2YIrO_6 crystallizes in monoclinic $P2_1/n$ space group with lattice parameters: $a = 5.7870(7)$ Å,

TABLE I. Crystal data and structure refinement for Sr_2YIrO_6 (a) subcell and (b) supercell at 293 K.

	(a) subcell	(b) supercell
Empirical formula	Sr_2YIrO_6	Sr_2YIrO_6
Formula weight	552.35	552.35
Temperature	293(2) K	293(2) K
Wavelength	0.71069 Å	0.71069 Å
Crystal system	monoclinic	cubic
Space group	$\text{P}2_1/n$	$\text{Fm}\bar{3}m$
Unit cell dimensions	$a = 5.7826(5)$ Å, $\alpha = 90^\circ$	$a = 8.1773(7)$ Å, $\alpha = 90^\circ$
	$b = 5.7830(5)$ Å, $\beta = 90.036(7)^\circ$	$b = 8.1773(7)$ Å, $\beta = 90^\circ$
	$c = 8.1746(7)$ Å, $\gamma = 90^\circ$	$c = 8.1773(7)$ Å, $\gamma = 90^\circ$
Volume	273.36(4) Å ³	546.80(14) Å ³
Z	2	4
Density (calculated)	6.710 g/cm ³	6.710 g/cm ³
Absorption coefficient	54.136 mm ⁻¹	54.129 mm ⁻¹
F(000)	480	960
Θ range for data collection	4.316 to 24.927°	4.317 to 26.846°
Crystal size	$0.042 \times 0.034 \times 0.033$ mm ³	$0.042 \times 0.034 \times 0.033$ mm ³
Reflections collected	1659	1128
Independent reflections	477 [$R_{int} = 0.0337$]	52 [$R_{int} = 0.0488$]
Completeness to $\Theta = 24.97^\circ$	97.9 %	97.6 %
Data / restraints / parameters	477 / 0 / 50	52 / 0 / 8
Goodness-of-fit	1.376	1.381
Final R indices [$> 2\sigma(I)$]	$R_{obs} = 0.0368^a$, $wR_{obs} = 0.0906^b$ $R_{obs} = 0.0135^a$, $wR_{obs} = 0.0359^b$	
R indices [all data]	$R_{all} = 0.0417^a$, $wR_{all} = 0.0919^b$ $R_{all} = 0.0165^a$, $wR_{all} = 0.0379^b$	

$$^a R = \sum || F_o | - | F_c || / \sum | F_o |$$

$$^b wR = \{ \sum [w(| F_o |^2 - | F_c |^2)^2] / \sum [w(| F_o |^4)] \}^{1/2}$$

TABLE II. Atomic coordinates ($\times 10^4$) and equivalent isotropic displacement parameters ($\text{\AA}^2 \times 10^3$) of Sr_2YIrO_6 (a) subcell and (b) supercell at 293(2) K with estimated standard deviations in parentheses.

(a) Sr_2YIrO_6 subcell	Wyck	x	y	z	Occupancy	U_{eq}^*
Y(1)	2d	0	5000	0	1	7(1)
Ir(1)	2d	5000	0	0	1	5(1)
Sr(1)	4e	5009(3)	5148(3)	2496(2)	1	17(1)
O(1)	4e	2380(2)	2100(3)	20(3)	1	59(7)
O(2)	4e	2980(3)	7300(3)	-180(3)	1	57(6)
O(3)	4e	4980(5)	-120(5)	2340(2)	1	84(8)
(b) Sr_2YIrO_6 supercell	Wyck	x	y	z	Occupancy	U_{eq}^*
Sr(1)	8c	2500	2500	2500	1	20(1)
Ir(1)	4b	5000	5000	5000	1	5(1)
Y(1)	4a	0	0	0	1	7(1)
O(1)	24e	5000	5000	7369(13)	1	85(5)

$b = 5.7912(6)$ \AA , $c = 8.1805(1)$ \AA , $\beta = 90.214(6)^\circ$ and $R_f = 2.11$, $R_{Bragg} = 2.01$ and reduced $\chi^2 = 2.32$. The result of the Rietveld refinement of the synchrotron XRD data using the cubic structural model discovered by single crystal XRD is depicted in Figure S3. Please note that both the monoclinic and the cubic model describe the synchrotron powder XRD data reasonably well with a slightly better fit by the monoclinic model (Bragg R-factor 2.11 for the monoclinic vs 3.46 for the cubic one). However, this difference is not significant since the larger number of fit parameters for the monoclinic model will yield better fit results as such. Hence, is very difficult to decide which model, monoclinic or cubic, is correct using powder diffraction data only. We emphasize that single crystal diffraction data is required to find the cubic $\sqrt{2}a \times \sqrt{2}b \times 1c$ supercell.

Figure 2 illustrates an SEM image of the Sr_2YIrO_6 single crystal, collected in backscattered electron (BSE) mode. EDX analysis was performed on various spots and on several crystals. The analysis suggests that the crystals are chemically homogeneous with a stoichiometry close to the target composition, within the accuracy of the EDX method.

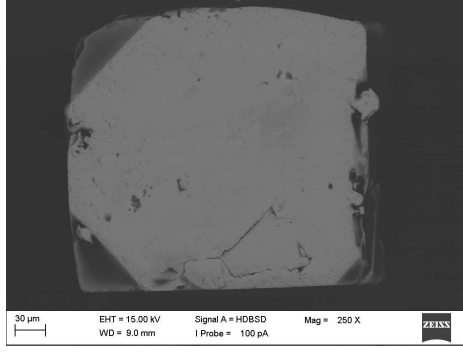


FIG. 2. SEM image of a typical Sr_2YIrO_6 single crystal in the backscattered electron (BSE) mode.

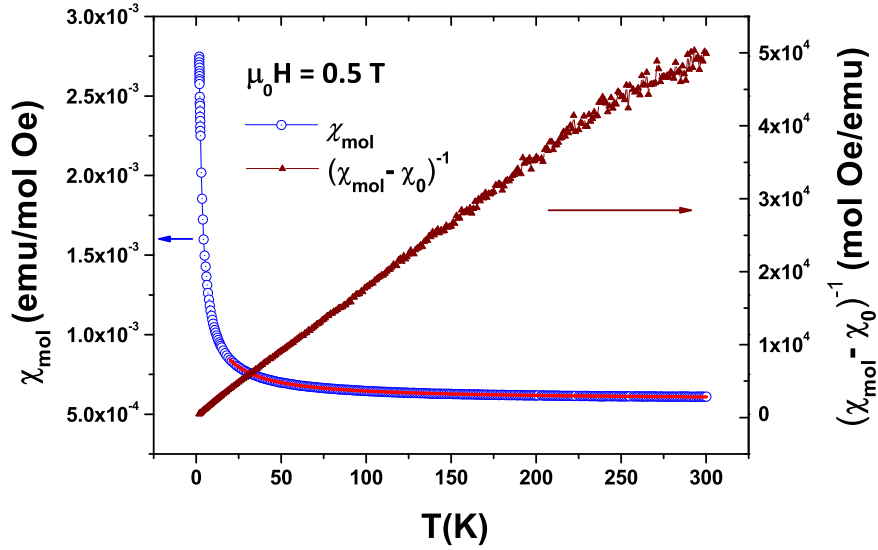


FIG. 3. (color online). The magnetic susceptibility of Sr_2YIrO_6 as a function of temperature in an external magnetic field $\mu_0 H = 0.5$ T, along with its fit according to a Curie-Weiss (CW) law in the temperature range 20-300 K (left axis). On the right axis, the inverse susceptibility (after subtracting χ_0 obtained from the CW fit) is plotted.

The magnetic susceptibility in an external magnetic field of $\mu_0 H = 0.5$ T is shown in Fig. 3 in the temperature range 1.8 -300 K, with no evidence of long-range magnetic order. The data obeys the Curie-Weiss law $\chi(T) = \chi_0 + C/(T - \Theta)$ in the temperature range 20 - 300 K, which gives a temperature independent susceptibility contribution $\chi_0 = 5.90 \times 10^{-4}$ emu/mol Oe, an effective magnetic moment $\mu_{eff} = 0.21\mu_B/\text{Ir}$, and a Curie-Weiss temperature $\Theta = -2.8$ K.

Due to the $5d^4$ electronic configuration of Sr_2YIrO_6 , a Van Vleck contribution to the susceptibility is expected: $\chi_0 = \chi_{Dia} + \chi_{VV}$, where χ_{Dia} comes from the diamagnetic contribution of the core levels and χ_{VV} is the Van Vleck paramagnetic susceptibility. The diamagnetic susceptibility can be obtained by adding the diamagnetic contribution of all the individual ions, leading to $\chi_{Dia} = -7.03 \times 10^{-5}$ emu/mol Oe, and finally $\chi_{VV} = 6.6 \times 10^{-4}$ emu/mol Oe, which is in agreement with similar $5d^4$ compounds [32, 33]. It is worth to notice that the obtained effective magnetic moment $\mu_{eff} = 0.21\mu_B/\text{Ir}$ is much smaller than the value $2.38\mu_B/\text{Ir}$ expected for a conventional $S = 1$ 5d-electron system as mentioned by Cao et al. [20], but it is in close agreement with the value $\mu_{eff} = 0.16\mu_B/\text{Ir}$ reported for polycrystalline Sr_2YIrO_6 [23]. As will be shown below, the paramagnetic signal can be attributed to a small percentage of paramagnetic centers (less than 1%), so it is likely that the Curie-tail in the magnetic susceptibility stems from paramagnetic impurities in the Sr_2YIrO_6 sample, only.

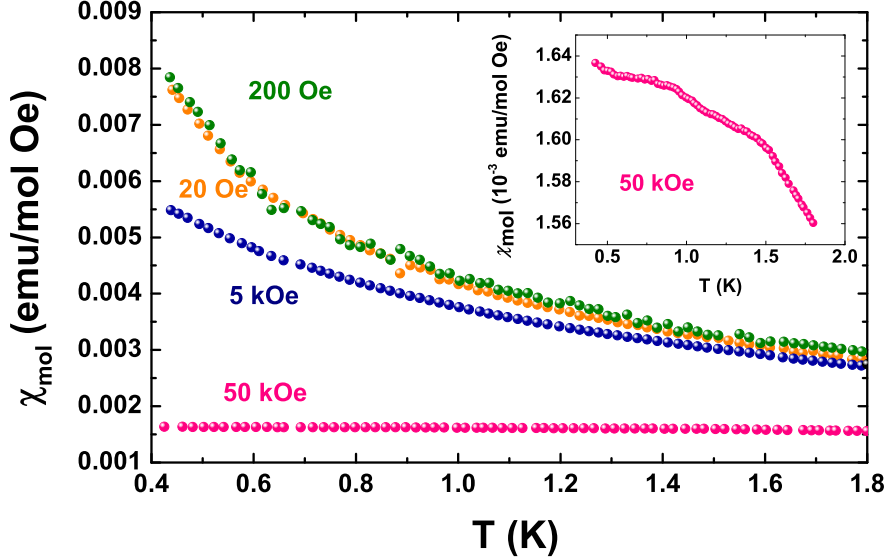


FIG. 4. (color online). Temperature dependence of the magnetic susceptibility in the low temperature region for different magnetic fields (ZFC results). The inset shows a zoom of the 5 T data down to 0.43 K.

In view of the antiferromagnetic transition at $T_N = 1.3$ K in 7 T magnetic field which has been observed in Ref. [20], we performed further magnetization studies at low temperatures and at high magnetic fields. From our experimental data no magnetic transition is detected

down to 0.43 K, even for applied magnetic fields up to 5 T (see Fig.4) [34].

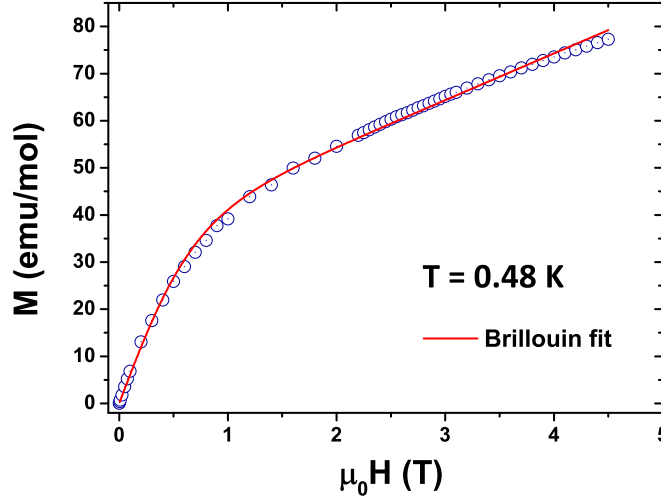


FIG. 5. (color online). Isothermal magnetization curve of Sr_2YIrO_6 at $T = 0.48$ K. The red line shows the fit according to the Brillouin function (for details see text).

The magnetization of Sr_2YIrO_6 as a function of applied magnetic field is shown in Fig. 5 for $T = 0.48$ K. In agreement with the temperature dependent measurements, the magnetic behavior at lowest temperatures is predominantly paramagnetic, and the curve can be fitted with the modified Brillouin function:

$$M(H) = \chi_0 H + n N_A g \mu_B J \left\{ \frac{2J+1}{2J} \coth \left(\frac{2J+1}{2J} \frac{g \mu_B J H}{k_B T} \right) - \frac{1}{2J} \coth \left(\frac{1}{2J} \frac{g \mu_B J H}{k_B T} \right) \right\}. \quad (1)$$

In this expression n represents a scaling factor which gives the percentage of paramagnetic Ir in the sample, N_A is the Avogadro constant, g the Landé factor, μ_B the Bohr magneton, J the total angular momentum, and k_B the Boltzmann constant. From the fit the parameters $g = 2.1$, and $\chi_0 = 9.9 \times 10^{-4}$ emu/mol Oe are found, together with a low percentage of paramagnetic centers ($J = 1/2$) of $n \sim 0.6\%$. These paramagnetic centers could be defects in the sample stemming from oxygen vacancies, chemical disorder (Y/Ir site mixing), off-stoichiometry, etc. A possible scenario could be the presence of Ir^{4+} or Ir^{6+} ions created by intermixing and/or off-stoichiometry [32, 35, 36].

The temperature independent susceptibility value χ_0 is slightly larger than the value ob-

tained from the Curie-Weiss fitting Fig. 3. This discrepancy could be due to non-negligible spin correlations at low temperature which are not included in Eq. 5, or to a temperature-dependent contribution to the Van Vleck susceptibility. It is worth to notice that no metamagnetic features arise in the field dependence of the magnetization in contrast to Ref. [20], where a sharp metamagnetic transition has been observed at the critical field $H_c \approx 2.6$ K at $T = 0.5$ K.

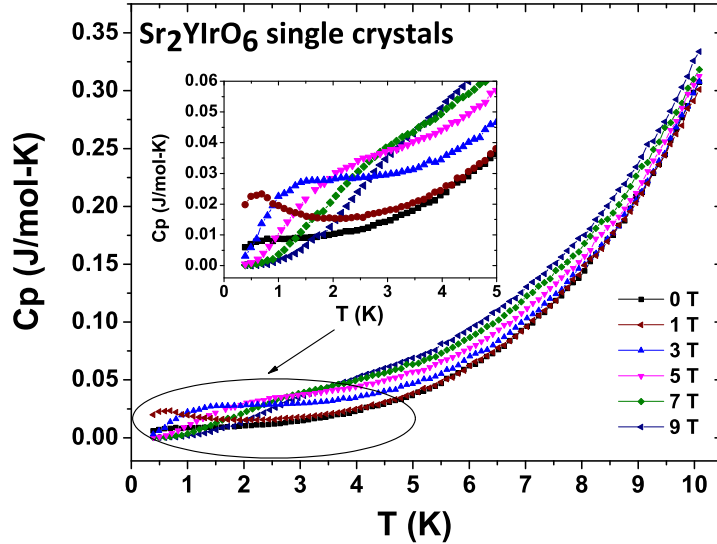


FIG. 6. (color online). Temperature dependence of the specific heat of Sr_2YIrO_6 for different magnetic fields, shown in the same scale as [20]. The inset shows a zoom into the low-temperature region.

The low temperature specific heat in different magnetic fields is shown in Fig. 6. A small anomaly is observed below $T \sim 5$ K in all the curves, including the zero-field data, and which becomes more pronounced in applied magnetic fields of 1, 3, and 5 T. This peak shifts to higher temperature and broadens with increasing magnetic fields, which in principle suggests its magnetic origin. However, its magnitude is small, and instead of being a sharp, λ -like anomaly, pointing towards a second-order phase transition, it resembles more a hump-like feature. This makes it difficult to identify the anomaly as a real magnetic phase transition.

In Ref. [20], Cao et al. detect a similar anomaly for their Sr_2YIrO_6 single crystals, in qualitatively and semi-quantitative agreement with the one observed here. In [20], the anomaly in the specific heat was interpreted as the onset of long-range magnetic order, due to its proximity to the ordering temperature $T_N = 1.3$ K observed as a sharp peak in the

magnetization as function of temperature. In order to settle this open question, we performed additional specific heat measurements on the non-magnetic cubic analog compound Ba_2YIrO_6 [32]. Since we observe striking similarities in our specific heat data for Sr_2YIrO_6 and Ba_2YIrO_6 [25], i.e. a broad anomaly below $T \sim 5$ K, it is rather improbable that the specific heat anomaly in Sr_2YIrO_6 marks a transition into a magnetically long-range ordered state.

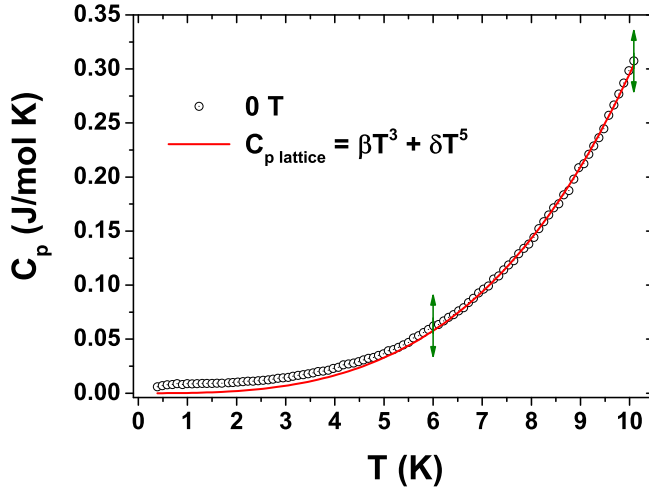


FIG. 7. (color online). Zero-field specific heat of Sr_2YIrO_6 . The red line represents the lattice specific heat obtained using a power-law fitting in the range of $6 \text{ K} \leq T \leq 10 \text{ K}$ marked by arrows; for details see text.

To gain a deeper insight into the origin of this anomaly, the lattice contribution was modelled for $6 \text{ K} \leq T \leq 10 \text{ K}$ using the approximation $C_{p,\text{lattice}} = \beta T^3 + \delta T^5$ in order to disentangle possible magnetic contributions in Sr_2YIrO_6 (Fig. 7). The extracted magnetic contribution shows a broad anomaly. From the fit parameters $\beta = 2.52 \times 10^{-4} \text{ J/mol K}^4$ and $\delta = 4.36 \times 10^{-7} \text{ J/mol K}^6$, the Debye temperature $\Theta_D = 425.7 \text{ K}$ was calculated. This value is comparable with those obtained for other double-perovskite materials [37, 38] and iridium-based compounds [33, 39].

Considering that the fitting range was small and chosen to follow the best-fitting procedure in combination with sufficient statistics, the extracted magnetic contribution to the specific heat has only a semi-quantitative character, i.e. the assumption $\Delta C_{p,\text{mag}} = 0$ for $T \geq 6 \text{ K}$ has been applied. Thus, in order to model the magnetic contribution to C_p in the following a subtraction of the zero-field data from the corresponding field data was per-

formed, yielding the field-dependent magnetic specific heat. The subtracted data are shown in Fig. 8(a). The shape of the $\Delta C_{p,mag}/T$ curves resembles a two-level Schottky anomaly, shifting to higher temperature with increasing magnetic field.

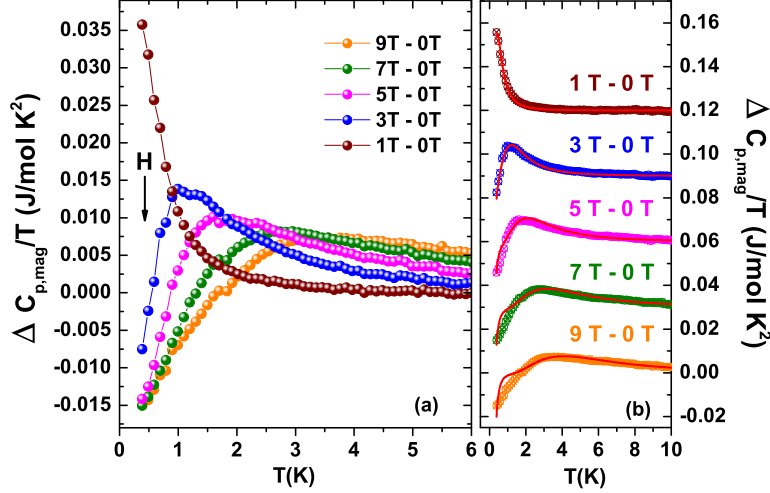


FIG. 8. (color online). (a) Temperature dependence of the low temperature specific heat divided by temperature for different magnetic fields, after subtraction of the zero-field data. (b) Experimental data from (a) represented with a constant offset of 0.03 J/mol K² for clarity. The red lines represent the fits according to a two-level Schottky anomaly (see text).

Consequently, the magnetic contribution shown in Fig. 8(a) was modelled as the subtraction of two Schottky anomalies, i.e. $C_m(T, H) = C_{Sch}(T, H) - C_{Sch}(T, 0)$. Following this reasoning, the peaks were fitted in the range $0.4 \text{ K} \leq T \leq 6 \text{ K}$ with the following expression:

$$C_m(T, H) = n \left[\left(\frac{\Delta(H)}{T} \right)^2 \frac{e^{\Delta(H)/T}}{(1 + e^{\Delta(H)/T})^2} - \left(\frac{\Delta_0}{T} \right)^2 \frac{e^{\Delta_0/T}}{(1 + e^{\Delta_0/T})^2} \right], \quad (2)$$

where n is the concentration of paramagnetic impurities, Δ_0 is the energy separation between the two levels in zero magnetic field, and $\Delta(H) = g\mu_B H$ represents the Zeeman splitting in an applied magnetic field H . The fits are shown in the Fig. 8(b). According to the fit, a value $\Delta_0 = 0.25 \text{ K}$ was found for the gap at zero field together with $n \approx 0.7 \%$, indicating that the anomaly is only based on a small amount of paramagnetic impurities, instead of being due to a real long-range magnetic ordering of all iridium atoms in Sr_2YIrO_6 .

While the fits reasonably describe our data for $H \leq 5 \text{ T}$, a slightly different behavior is found for $H \geq 7 \text{ T}$ with a lacking peak at low temperatures in our experimental data. This

suggests that even when a Schottky anomaly can explain the observed peaks for $H \leq 5$ T (low fields), for higher fields the magnetic contribution is altered. Following the discussion about the Brillouin fitting in Fig. 5, this could point towards field-induced changes, possibly due to non-negligible spin correlations from correlated magnetic impurities which, nonetheless, are not associated with long-range magnetic ordering, but with short-range correlations only. The possibility of magnetic correlations due to impurities was already pointed out for polycrystalline $\text{Ba}_{2-x}\text{Sr}_x\text{YIrO}_6$ [23] and Ba_2YIrO_6 single crystals [32].

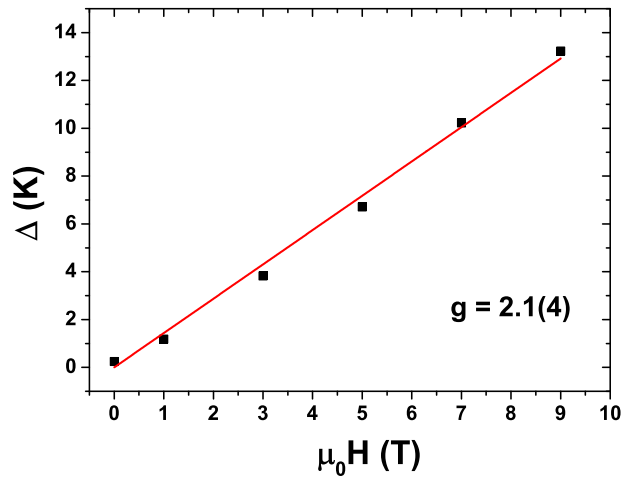


FIG. 9. (color online). Magnetic field dependence of the energy gap between the ground state doublet for paramagnetic impurity spins in Sr_2YIrO_6 . The red line and the g value are the fitting results using $\Delta = g\mu_B H$.

We emphasize the fact that both the paramagnetic susceptibility and the Schottky two-level anomaly can be ascribed to the presence of correlated impurity spins Ir^{4+} or Ir^{6+} . With this in mind, the Zeeman splitting between the two lowest energy levels obtained from the former fits can be plotted as a function of applied magnetic field (see Fig. 9). From $\Delta = g\mu_B H$ the Landé g factor was found to be $g = 2.1(4)$, which is consistent with the g factor obtained from the Brillouin fit, $g = 2.1(0)$.

Finally, we can evaluate the magnetic entropy S_{mag} for our samples by integrating the zero-field specific heat data from Fig. 7 according to the expression:

$$S_{mag} = \int_0^T \frac{C_{mag}}{T} dT. \quad (3)$$

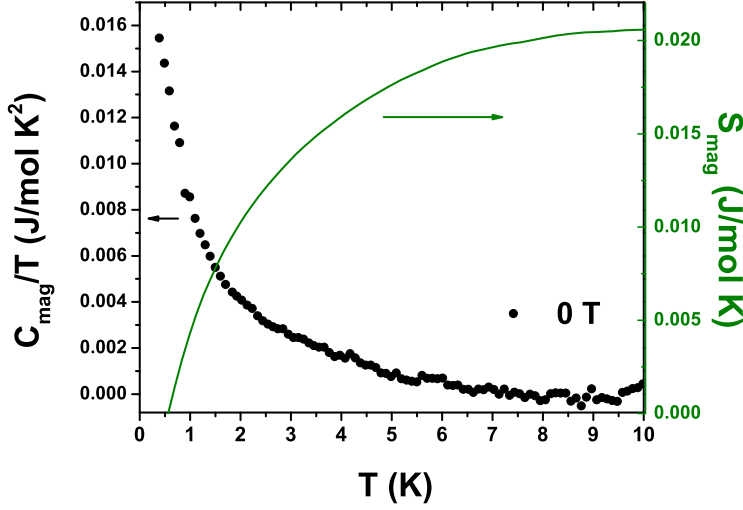


FIG. 10. (color online). Zero-field magnetic specific heat plotted as $C_{p,mag}/T$ vs T (left scale) together with the magnetic entropy (right scale).

The resulting curves for $C_{p,mag}/T$ and $S_{mag}(T)$ are shown in Fig. 10. The small value $S_{mag} = 0.021$ J/mol K is of the same order of magnitude as reported by Cao et al. [20] (~ 0.01 J/mol K). This non-zero value again points to the presence of paramagnetic impurities, which need to be taken into account. For a $S = 1/2$ ground state of Sr_2YIrO_6 as claimed in Ref. [20], a total entropy $S_{mag} = R \ln(2J + 1) = R \ln(2) = 5.76$ J/mol K is expected, which is evidently far from the experimental observations. Nevertheless, considering the small and finite number of n impurities in our samples with presumably $J = 1/2$ contributing to the magnetic entropy, we have $S_{mag} = 0.021$ J/mol K $= nR \ln(2)$, and therefore $n \sim 0.4\%$. Overall, our magnetic and thermodynamic characterization is consistent with a non-magnetic ground state of Sr_2YIrO_6 with the presence of a small amount of correlated $J = 1/2$ paramagnetic centers. From our results, it is clear that the low temperature specific heat anomalies are not related with the onset of long-range magnetic order.

IV. CONCLUSIONS

Following a recent matter of debate as to the evolution of magnetism in monoclinic Sr_2YIrO_6 , we have grown single crystals of Sr_2YIrO_6 using anhydrous SrCl_2 flux. Our single crystal XRD results shows for the first time the presence of a $\sqrt{2}a \times \sqrt{2}a \times 1c$ supercell,

where a , b and c are the unit cell dimensions of the monoclinic subcell, highlighting the cubic supercell of this compound.

The magnetic susceptibility revealed a predominantly paramagnetic behavior in the temperature range $0.4 \text{ K} < T \leq 300 \text{ K}$ with an effective magnetic moment $\mu_{eff} = 0.21\mu_B/\text{Ir}$ and non-negligible but small spin correlations. From the Brillouin fit for the isothermal magnetization curve at $T = 0.48 \text{ K}$ a low percentage of $J = 1/2$ impurities were identified as the source for the observed paramagnetism. No long-range magnetic ordering was observed down to 430 mK .

A thorough study of the specific heat was carried out, in which a broad anomaly in the low temperature region $T \leq 5 \text{ K}$ was identified as a Schottky anomaly caused by paramagnetic impurities present in the sample, which are of the same order of magnitude ($n \sim 0.4 - 0.7 \%$) as obtained from magnetization measurements. Our results are in strong contrast with the reported ones by Cao et al. [20], but in full agreement with recent reports on polycrystalline samples [23, 24], pointing towards a non-magnetic ground state with the presence of a small amount of correlated $J = 1/2$ impurities.

ACKNOWLEDGMENTS

The authors would like to thank M. Vojta, D. Efremov, J. van den Brink and J. Wosnitzer for fruitful discussions. This work has been supported by the Deutsche Forschungsgemeinschaft DFG under SFB 1143 and the Emmy-Noether program (Grant No. WU595/3-3).

REFERENCES

-
- [1] J. G. Rau, E. Kin-Ho Lee and Hae-Young Kee, *Annu. Rev. Condens. Matter Phys.* 7:2:1-2.27 (2016)
 - [2] W. Witczak-Krempa, G. Chen, Y. Baek Kim and L. Balents, *Annu. Rev. Condens. Matter Phys.* 5:57-82 (2014)
 - [3] A. Nag, S. Middey, S. Bhowal et al., *Phys. Rev. Lett.* 116, 097205 (2016)

- [4] S. Chikara, O. Korneta, W. P. Crummett, L. E. DeLong, P. Schlottmann, and G. Cao, Phys. Rev. B 80, 140407(R) (2009)
- [5] M. Ge, T. F. Qi, O. B. Korneta, D. E. De Long, P. Schlottmann, W. P. Crummett and G. Cao, Phys. Rev. B 84, 100402(R) (2011)
- [6] Y. Chen and H. Y. Kee, Phys. Rev. B 90, 195145 (2014)
- [7] G. Jackeli and G. Khaliullin, Phys. Rev. Lett. 102 017205 (2009)
- [8] D. Pesin and L. Balents, Nat. Phys. 6, 376 (2010)
- [9] X. Wan, A. M. Turner, A. Vishwanath, S. Y. Savrasov, Phys. Rev. B 83, 205101 (2011)
- [10] W. Witczak-Krempa and Y. B. Kim, Phys. Rev. B 85, 045124 (2012)
- [11] A. A. Burkov and L. Balents, Phys. Rev. Lett. 107, 127205 (2011)
- [12] W. Witczak-Krempa, T. P. Choy, Y. B. Kim, Phys. Rev. B 82, 165122 (2010)
- [13] M. Kargarian, J. Wen, G. A. Fiete, Phys. Rev. B 83, 165112 (2011)
- [14] X. Wan , A. Vishwanath, S. Y. Savrasov, Phys. Rev. Lett. 108, 146601 (2012)
- [15] A. Go, W. Witczak-Krempa, G. S. Jeon, K. Park, Y. B. Kim, Phys. Rev. Lett. 109, 066401 (2012)
- [16] N. N. Greenwood and A. Earnshaw, *Chemistry of the elements*, Elsevier-Butterworth-Heinemann, Amsterdam (2012)
- [17] G. Chen, R. Pereira and L. Balents, Phys. Rev. B 82, 174440 (2010)
- [18] B. J. Kim, H. Jin, S. J. Moon, J.-Y. Kim et al., Phys. Rev. Lett. 101, 076402 (2008)
- [19] M. Wakeshima, D. Harada, Y.J. Hinatsu, J Alloys Compd. 287, 130 (1999)
- [20] G. Cao, T. F. Qi, L. Li, J. Terzic et al., Phys. Rev. Lett. 112, 056402 (2014)
- [21] S. Bhowal, S. Baidya, I. Dasgupta and T. Saha-Dasgupta, Phys. Rev. B 92, 121113(R) (2015)
- [22] K. Pajskr, P. Novák, V. Pokorný, J. Kolorenč, R. Arita and J. Kuneš, Phys. Rev. B 93, 035129 (2016)
- [23] B. Ranjbar, E. Reynolds, P. Kayser and B. J. Kennedy, Inorg. Chem. 54, 10468 (2015)
- [24] B. F. Phelan, E. M. Seibel, D. Badoe Jr., W. Xie, R. J. Cava, Solid State Commun. 236, 37 (2016)
- [25] See Supplemental Material at [URL will be inserted by publisher]
- [26] X-AREA; X-SHAPE; X-RED STOE & Cie GmbH: Darmstadt, Germany (2004)
- [27] Sheldrick, G. M. SHELXTL, version 5.1, University of Göttingen: Göttingen, Germany, (1997)

- [28] Petříček, V.; Dušek, M.; Palatinus, L. Jana, The crystallographic computing system; Institute of Physics: Prague, Czech Republic, (2006)
- [29] A.-C. Dippel, H.-P. Liermann, J. T. Delitz et al., Journal of Synchrotron Radiation, 22, 3, 675-687 (2015)
- [30] H. M. Rietveld, J. Appl. Cryst. 2, 65 (1969)
- [31] T. Roisnel, J. Rodriguez-Carjaval, Mater. Sci. Forum 378-381, 118 (2001)
- [32] T. Dey, A. Maljuk, D. V. Efremov, O. Kataev, et al., Phys. Rev. B 93, 014434 (2016)
- [33] M. Bremholm, S. E. Dutton, P. W. Stephens, and R. J. Cava, J. Solid State Chem. 184, 601 (2011)
- [34] Note that the tiny humps in the 5 T curve are due to technical artifacts which are arising from the combination of the large number of data points and negligible changes in the susceptibility in the shown temperature regime.
- [35] P. Kayser, M. J. Martínez-Lope, J. A. Alonso, M. Retuerto, M. Croft, A. Ignatov, and M. T. Fernández-Díaz, Inorg. Chem. 52, 11013 (2013)
- [36] A Brillouin function with $J = 3/2$ also allows to fit the data. However, this fit leads to non-consistent, too low g values.
- [37] Y. Du, Z.X. Cheng, S. X. Dou, X. L. Wang, H. Y. Zhao and H. Kimura, App. Phys. Lett. 97, 122502 (2010)
- [38] C.G.F. Blum, A. Holcombe, M. Gellesch et al., J. Cryst. Growth 421, 39 (2015)
- [39] Y. Cai, Y. Li and J. Cheng, “Synthesis, Crystal Structure, and Physical Properties of the Perovskite Iridates” in *Perovskite Materials - Synthesis, Characterisation, Properties, and Applications*, InTech (2016)